The $(t,{}^3\mathrm{He})$ reaction at 43 MeV/nucleon on ^{48}Ca and ^{58}Ni: Results and microscopic interpretation

J. Guillot, S. Galès, D. Beaumel, S. Fortier, E. Rich, and N. Van Giai
Institut de Physique Nucléaire, IN2P3-CNRS, F-91406 Orsay, France

G. Colò
Dipartimento di Fisica, Università degli Studi and INFN sez. di Milano, via Celoria 16, I-20133 Milano, Italy

A. M. van den Berg, S. Brandenburg, B. Davids, M. N. Harakeh, M. Hunyadi,* M. de Huu, S. Y. van der Werf, and H. J. Wörtche
Kernfysisch Versneller Instituut, NL-9747 AA Groningen, The Netherlands

C. Bäumer, D. Frekers, E.-W. Grewe, P. Haefner, and B. C. Junk
Institut für Kernphysik, Universität Münster, D-48194 Münster, Germany

M. Fujiwara
Research Center for Nuclear Physics, Osaka University, Ibaraki, Osaka 567-0047, Japan, and
Advanced Photon Research Center, Japan Atomic Energy Institute, Kizu, Kyoto 619-0215, Japan
(Received 14 January 2005; published 31 January 2006)

We have used the 43 MeV/nucleon primary tritium beam of the AGOR facility with an intensity of 4×10^7 pps and the BBS experimental setup to study the $(t,{}^3\mathrm{He})$ reaction between 0° and 5° lab angles on ^{12}C, ^{48}Ca, and ^{58}Ni targets. The standard ray-tracing procedure has allowed us to obtain excitation-energy spectra up to 30 MeV in six angular bins for each residual nucleus, with an average energy resolution of 350 keV. The reaction mechanism has been described in distorted-waves Born approximation (DWBA) using the DWBA98 code. In this approximation, the form factor is treated as a folding of an effective projectile-nucleon interaction with a transition density. The effective projectile-nucleon interaction has been adjusted to reproduce the 0° cross section of the 1^+ ground state of ^{12}B populated in the $^{12}\mathrm{C}(t,{}^3\mathrm{He})$ reaction. We have employed random-phase approximation (RPA) wave functions of excited states to construct the form factor instead of the normal modes wave functions used earlier. This new DWBA+RPA analysis is used to compare calculated and experimental cross sections directly and to discuss the giant resonance excitations in ^{48}K and ^{58}Co nuclei.

DOI: 10.1103/PhysRevC.73.014616 PACS number(s): 24.30.Cz, 25.55.Kr, 27.20.+n, 27.40.+z

I. INTRODUCTION

Except for the giant dipole resonance (GDR), the systematics of the isovector giant resonances are basically unknown, especially for the isovector monopole. This $L = 0$ resonance is interesting because of its role in isospin mixing and its importance in determining the symmetry term of the equation of state of nuclear matter as well as the isospin terms of the effective nucleon-nucleon interaction. Although the isovector ($\Delta T = 1$) non-charge-exchange ($\Delta T_z = 0$) giant dipole resonance (IVGDR) is the oldest and best known resonance, and systematic information is available for isoscalar ($\Delta T = 0$) resonances such as monopole or quadrupole resonances, the clear identification and unambiguous L-assignment of the 1 or $2\hbar\omega$ isovector giant resonances (IVGRs) in the charge-exchange ($\Delta T = 1$, $\Delta T_z = \pm 1$) sector constitutes a long-standing experimental problem [1]. In particular in the excitation energy range where the monopole collective strength was expected, either $L = 0$ and/or $L = 2$ transitions have been observed [2] depending on the reaction. Moreover, these resonances are often identified after subtraction of a very large continuum background, adjusted to connect smoothly to the high-excitation-energy part of the spectra. Recently, strong evidence has been found for the location of the isovector spin giant monopole resonance (IVSGMR) in ^{208}Pb in an exclusive $({}^3\mathrm{He},tp)$ experiment at 410 MeV [3]. Concerning the $L = 0$, $S = 1$ $0\hbar\omega$ IVGR, the GT resonance, it has only recently been experimentally shown to almost fully exhaust the sum rule from the studies of the (p,n) and (n,p) reactions [4].

In the present article we try mainly to answer the two following questions: Where is the monopole resonance and what amount of strength can be observed in ^{48}K and ^{58}Co via the τ_+ channel? To compensate for the lack of really selective probes, we have chosen to use the $(t,{}^3\mathrm{He})$ reaction at 130 MeV. We were guided by several considerations in the choice of this experiment. The τ_+ channel in such a (n,p)-like reaction leads to excitation of only one isospin component, $T = T_0 + 1$, where T_0 is the isospin of the ground state of the target nucleus. This is in contrast to inelastic scattering reactions or (p,n)-like reactions. Moreover, the $T_0 + 1$ component of IVGRs is located at a lower excitation energy compared to its location in the τ_0 and τ_- channels, leading to a smaller spreading width. At a bombarding energy of 43 MeV/nucleon, the V_τ term of the NN interaction is comparable to the $V_{\sigma\tau}$ term [5], but the spin-flip transitions are still dominant over

*On leave from the Institute of Nuclear Research of the Hungarian Academy of Sciences, Debrecen, Hungary.

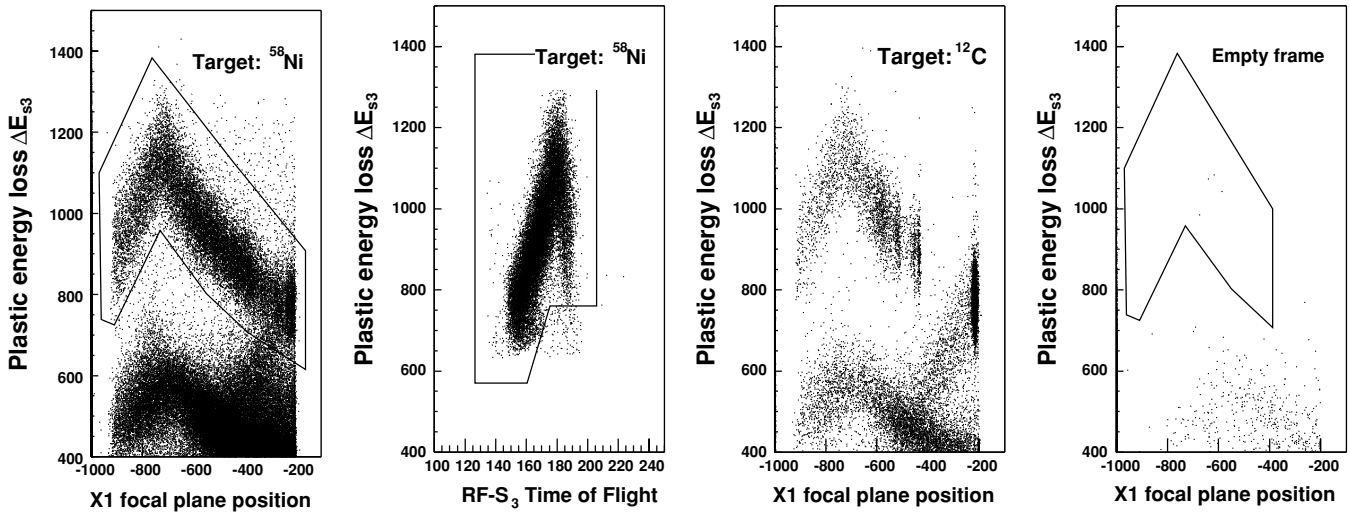

FIG. 1. ^{3}He identification on Ni, C targets and an empty frame with the BBS spectrometer at 0°. All quantities are plotted as a function of channel number.

the non-spin-flip ones because of the statistical factor (=3) connected with the $\Delta S = 1$ channel. Interesting features of the present study using the $(t,{}^3\mathrm{He})$ reaction are the expected surface-peaked nature of the reaction and the fact that $L = 0$ transitions should be enhanced at very forward angles.

After discussing a standard distorted-waves Born approximation (DWBA) analysis of the experimental data, we present a new microscopic approach based on random-phase approximation (RPA) calculations.

II. EXPERIMENTAL SETUP

A. Triton beam production

Efforts made in the past 3 years at KVI to develop a primary tritium beam have been quite successful [6]. Low-intensity triton beams, produced with the ECR ion source, are injected and accelerated in the superconducting accelerator AGOR. The gas, consisting of a mixture of deuterium and tritium (22 ppm tritium), is stored as uranium hydride, from which it is liberated by heating and it flows into the plasma source through a calibrated leak. The gas flow is controlled by varying the temperature and thereby the pressure. The optimization of the beam settings is done with $^3\mathrm{He}^{1+}$ ions. The switch to a triton beam then necessitates the installation of two stripper foils at the exit of the cyclotron, before the first bending magnet and between the first and second bending magnets, respectively, to suppress the spurious incident $^3\mathrm{He}^{1+}$ ions. In the present experiment, the final triton beam had an incident energy of 130 MeV and an intensity of 4×10^7 pps on target.

B. Detection and identification of ^{3}He ions

Enriched self-supporting targets of 4.7 mg/cm^2 thickness ^{58}Ni and 17 mg/cm^2 thickness ^{48}Ca were used, together with a ^{12}C target and also an empty frame to check for impurities or spurious events. The targets were always positioned in the plane perpendicular to the incident beam. ^{12}C impurities were negligible in the targets but a hydrogen contamination gave rise to spurious peaks in the low-excitation-energy part (up to 6 MeV) during the measurements on the ^{58}Ni target.

The ^{3}He ejectiles were detected in the big-bite magnetic spectrometer (BBS) [7] equipped with its focal-plane detection system [8]. A thin plastic scintillator (S3) was inserted between the vertical drift chambers and the two standard plastic scintillators. Owing to the factor of two between the magnetic rigidity of the ejectile and that of the projectile, a very clean identification of the interesting ^{3}He ions could be achieved, even with the BBS at 0°, as illustrated in Fig. 1.

Figure 1 shows two-dimensional plots of the energy loss in S3 versus focal plane position X for ^{58}Ni, ^{12}C, and an empty target and versus cyclotron RF-S3 time of flight in the case of ^{58}Ni. Both plots are used to select the ^{3}He ejectiles.

The BBS backtracking procedure allows us to extract the differential cross sections in narrow angular ranges. We have chosen an angular binning of 0.7° width rings (around 0°) or ring sections (around 5°) in the (θ_t, ϕ_t) target plane, leading to six measurements around 0.35°, 1.05°, 1.55°, 4.3°, 5°, and 5.6° in the laboratory. These angles are often referred to by the numbers 1 to 6, respectively, in the text. Typical residual spectra of the total 0° measurements are presented in Fig. 2. The spectra obtained with ^{48}Ca and ^{58}Ni targets suggest an overlap of many structures above 5 and 9 MeV excitation energy, respectively.

III. DWBA ANALYSIS AND REACTION MECHANISM CONSIDERATIONS

Although the distorted-waves impulse approximation (DWIA) can be used to describe the reaction mechanism at higher incident energy, we have to take into account distortion effects by using a DWBA analysis with the DWBA98 code [9].

A. DWBA98 code common inputs

In the framework of the prior form of the DWBA, the transition matrix element can be written as follows:

$$T_{fi} = \langle \chi_f^+ | F(\vec{R}; E) | \chi_i^- \rangle, \quad (1)$$

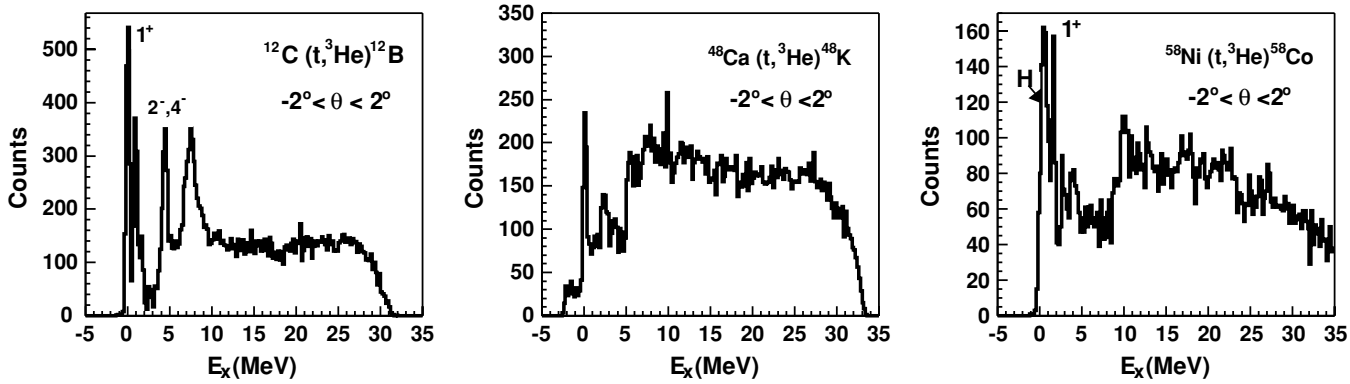

FIG. 2. ^{12}B, ^{48}K, and ^{58}Co excitation energy spectra obtained in the (t,^{3}He) reaction at $E_t = 130$ MeV.

where the form factor $F(\vec{R}; E)$ is the folding of the transition density with an effective projectile-nucleon (N-proj) interaction:

$$F(\vec{R}; E) = \int d^3r\, V_{\text{eff}}^{(N\text{-proj})}(\vec{r} - \vec{R})\delta\varrho(\vec{r}; E), \qquad (2)$$

and where χ_i^- and χ_f^+ are the incoming and outgoing distorted waves.

The quantity $\delta\varrho$ represents the change in density associated with the excitation of a state at energy E in the target. Alternatively, if we introduce a transition density for the projectile as well, we can write the form factor as the double folding of an effective nucleon-nucleon interaction with the two transition densities.

1. Optical-potential choices and distorted-wave functions

In the same way as was commonly done for the (^{3}He,t) reaction, the ^{3}He optical potentials were chosen from those fitting the elastic scattering at 130 MeV measured in previous experiments over a large angular range, and a 15% reduction of the real and imaginary depths of the ^{3}He optical potential was applied to construct the tritium channel optical potentials. This procedure of a 0.85 scaling factor between the t and the ^{3}He optical potentials has been found to fit the data reasonably well [10] and avoids the proliferation of free parameters and has been applied for every nucleus.

In the present experiment the measured angular range is too narrow to allow a more relevant statement on the determination of the optical potential parameters and we have compared parameters already determined in previous experiments especially dedicated to this aspect.

In the case of ^{58}Ni, the choice of an optical potential with an imaginary surface term has been preferred to a volume one among those given in Ref. [11] because of the better fit of the angular distribution of the GT 1^+ group of levels around $E_x = 1.8$ MeV. For this nucleus, the comparison between two optical potentials with such an imaginary surface term, the optical potential given in Ref. [11] and the energy-mass-dependent (EMD) potential [12], gives values of 1.03, 0.91, and 0.88 for the ratio between their 0° cross sections for 0^+, 1^+, and 2^- states, respectively, and a value of 0.90 at 3.5° where this last 2^- cross section is maximum. We thus estimate that the optical potential sensitivity is ≈10% in this case. These calculations were made with a size parameter value $\hbar\omega = 41\,\text{A}^{-1/3}$ MeV. The same size parameter has been used for every nucleus and for the normal mode wave functions (defined in Sec. III B1) in this article.

In the case of ^{48}Ca, the energy-mass-dependent (EMD) potential [12] and a potential deduced from ^{40}Ca elastic scattering studies [13], with a small isospin correction for ^{48}Ca, give similar results for the 2^- ground state in our angular range. We have adopted the first one for its imaginary surface term.

In the case of ^{12}C, which has been used for the calibration of the effective interaction (see Sec. III A3), we have taken the optical potential obtained in the analysis of 119 MeV ^{3}He elastic scattering data [12].

The ^{3}He optical potentials finally retained for the analysis are given in Table I.

2. Effective t-N interaction

In the DWBA98 code, a phenomenological effective interaction can be used. Here, we do not introduce a transition density for the projectile but an effective interaction that is expressed as a sum over Yukawa terms as in the (p,n) case.

$$\begin{aligned} V_{\text{eff}}(r) = [&V_\tau Y(r/R_\tau) + V_{\sigma\tau} Y(r/R_{\sigma\tau})(\vec{\sigma}_1 \cdot \vec{\sigma}_2) \\ &+ V_{LS\tau} Y(r/R_{LS\tau})\vec{L} \cdot \vec{S} \\ &+ V_{T\tau} r^2 Y(r/R_{T\tau}) S_{12}](\vec{\tau}_1 \cdot \vec{\tau}_2). \end{aligned} \qquad (3)$$

TABLE I. ^{3}He optical-model parameters used in this work.

Nucleus	V_0 (MeV)	W_D (MeV)	r_V (fm)	r_{WD} (fm)	a_V (fm)	a_{WD} (fm)	r_C (fm)	Ref.
^{12}C	106.48	15.64	1.032	1.133	0.808	0.787	1.30	[12]
^{48}Ca	97.80	21.50	1.210	1.170	0.760	0.816	1.30	[12]
^{58}Ni	100.00	20.20	1.211	1.180	0.805	0.817	1.30	[11]

The same effective interaction has been commonly used in the analysis of the (^{3}He,t) reaction at different incident energies and of the (t,^{3}He) reaction at higher incident energy [14]. In this approximation the folding with the interactions of the exchanged nucleon and the spectator nucleons in the projectile is not explicitly introduced but is taken into account only phenomenologically within the values of the different terms. In the same way, the *LS* term is assumed to be small and is also ignored. The determination of this *LS* term would need experiments with polarized beams, which have not yet been done, but it would be interesting to have better knowledge of it. Here we have used only the V_τ, $V_{\sigma\tau}$, and $V_{T\tau}$ terms in our approximation.

The ranges of the different terms are chosen near to the OPEP values [15] as usual, and only their depths were adjusted in the present analysis.

The V_τ term is the best known and its energy dependence has been determined by comparing experimental cross sections to theoretical predictions in (^{3}He,t) reactions at different energies [16]. We have interpolated it at our energy to a value of 5 MeV to take into account this well-established energy dependence. It is important to remark that this term varies rapidly at low energy. The $V_{\sigma\tau}$ and $V_{T\tau}$ terms are much less well established.

3. *Calibration of the effective interaction on the* 1^+ *ground state of* ^{12}B

We present in Table II two different parameter sets that have been used in our analysis. As shown in Fig. 3 the first one reproduces the angular distribution of the 1^+ G.S. level of ^{12}B rather well with a renormalization by a factor of 1.3 at 0°. The wave function used here for this level is from the Cohen and Kurath model [17]. One should note that an increase of 30% of the imaginary term in the optical potentials reduces the calculated cross section at 0° by 12% and at 8° by 18%.

The second set is deduced from a previous systematic analysis in the 22–30 MeV/nucleon range [18] with the V_τ term fixed to 5 MeV at our energy. It does not reproduce the differential cross section shape for the 1^+ G.S. level of ^{12}B cross section quite as well but overestimates its 0° cross section rather less (by 10%).

The shell-model wave function of the 1^+ state calculated by Kawabata [19], including not only p but also s-d shells, gives no significant difference on the shape but increases the absolute cross section by 20% and may thus slightly affect the choice of the effective interaction terms. This 1^+ state is, moreover, not only sensitive to $V_{\sigma\tau}$ but also to $V_{T\tau}$. One would thus need other states such as stretched states with a high spin and a well-known wave function to constrain $V_{T\tau}$ better. We could not isolate such a state in the present data.

TABLE II. Effective t-N interaction sets for the (t,^{3}He) reaction at 130 MeV.

Effective interaction	V_τ (MeV)	$V_{\sigma\tau}$ (MeV)	$V_{T\tau}$ (MeV)
Set I	5.00	−4.10	−6.00
Set II	5.00	−3.00	−6.50

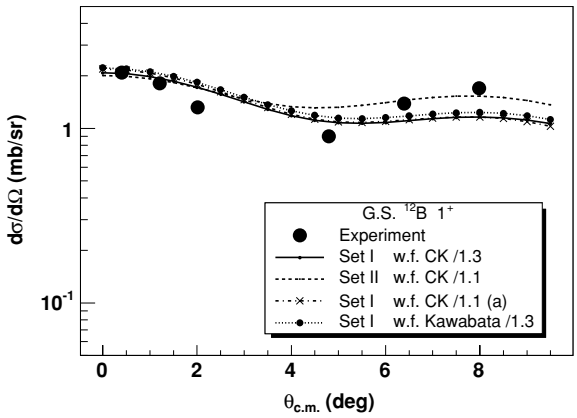

FIG. 3. ^{12}B 1^+ ground-state angular distribution; w.f. CK stands for the Cohen and Kurath wave function; and (a) denotes a modified imaginary part of the optical potentials (see text).

We prefer the first set because it is in better agreement with the fact that in this region of incident energy per nucleon, the $V_{\sigma\tau}$ and V_τ terms are of comparable strength in the *NN* interaction. We can deduce from these comparisons that the sensitivity to the effective interaction is ≈10% in the case of this 1^+ state.

B. Nuclear structure input

1. *Standard normal modes wave functions*

In the standard analysis, the excited final states can be built from the most possible coherent superposition of $1p1h$ states. These collective wave functions in the so-called normal modes (NM) are obtained by applying an operator O^μ_{LJM} (resembling an electromagnetic operator in the spin-space part but carrying a $t_\pm$ isospin part) to the harmonic oscillator wave functions describing the initial state. This was done using the NORMOD code developed by Van der Werf [20]. The initial state $|0\rangle$ is described with the filling of the successive shells and the upper empty shells can be chosen as a basis for the $1p1h$ states in the appropriate way to select the desired $\Delta N\hbar\omega$ transitions (see, for example, Ref. [21] for a detailed description).

One has to distinguish between non-spin-flip and spin-flip transitions. The operators O^μ_{LJM} are

$$O^\mu_{(L=J)JM} = \sum_i r_i^J Y_{JM}(\hat{r}_i) t_\mu(i) \tag{4}$$

and

$$O^\mu_{LJM} = \sum_i r_i^L [Y_L(\hat{r}_i) \otimes \sigma_i]_{JM} t_\mu(i). \tag{5}$$

In the case of spin-flip transition, L can be J or $J \pm 1$. In the harmonic oscillator basis, the excited states are

$$|LJM\rangle = \sum_{ph} Z^{LJM}_{ph} [a^\dagger_p a_h]_{LJM} |0\rangle, \tag{6}$$

where

$$Z^{LJM}_{ph} = \langle ph; LJM | O^\mu_{LJM} | 0\rangle \Big/ \sqrt{\sum_{ph} |\langle ph; LJM | O^\mu_{LJM} | 0\rangle|^2}. \tag{7}$$

It is obvious that such a normal-mode wave function exhausts the corresponding non-energy-weighted sum rule. Associating this with observed experimental strength makes sense provided that all this strength is located within a small energy region. An extension of the NM method for the search of collective strength over a wide excitation energy range has been commonly used via multipole decomposition analysis (MDA). The experimental spectra are divided in energy bins (typically 1 MeV wide) where the difference between the experimental cross section and the weighted sum of multipole cross sections calculated using NM wave functions is minimized (see Sec. IV A). In this procedure the form factor is kept constant over the whole energy range and the excitation energy dependence relies only on the Q-value change in the exit channel. This means that in such analysis the correlation between excitation energy and nuclear structure is omitted by definition. Moreover, this is a fitting procedure that introduces its own artifacts depending on the number of experimental measurements and on the number of multipoles included in the fit. The nuclear spectrum associated with a given multipolarity is composed of both collective and noncollective excitations. Therefore, in the experimental analysis it may be a dangerous assumption to use a collective transition density or form factor at each energy E from zero to the maximum energy available in the measurement.

This issue has been discussed in a number of cases: for instance, in the case of the isoscalar giant monopole resonance (ISGMR) a possible overestimation of the energy-weighted sum rules and shifts of centroid energies because of the collective-model-based DWBA reaction description has been reported previously [22]. It has also been pointed out recently that in the case of the isoscalar giant dipole resonance (ISGDR), although essentially all theoretical models predict that at low energy noncollective strength exists, the experimental analysis is based on the use of constant form factors at different energies (see, e.g., Ref. [23] and references therein).

2. Microscopic RPA wave functions

We do not have yet a sufficient database to judge the effect of the approximation based on using energy-independent, collective transition densities in the DWBA calculation. We have tried in our work to study this problem by complementing the NM analysis with another calculation in which the transition densities at each energy come from a microscopic RPA calculation. We feel motivated also by the fact that a recent similar RPA calculation for ^{208}Pb, coupled to a Glauber-type model for the reaction cross sections, has given enlightening results in connection with our present problem (the IVGMR) but in the case of a different reaction, namely (^{13}C,^{13}N) [24]. We believe that the coupling of fully microscopic structure and reaction models should be pursued more extensively.

Charge-exchange RPA is a well-known method, and many studies have been carried out within this framework, starting with the work of Auerbach and Klein [25]. We recall here the main characteristics of this type of calculation and we report some details for the present one, which are given along the lines of Ref. [26]. The calculation is self-consistent in the sense that the residual proton-neutron particle-hole interaction is derived from the Skyrme force used to build the ground state. We have chosen the Skyrme parametrization SGII [27].

In our method, we first solve the Hartree-Fock (HF) equations in the coordinate space and we obtain the mean field. Radial integrals are computed up to a maximum radial distance of 18 fm, using a mesh of 0.1 fm. The unoccupied states, including those at positive energies, are obtained by diagonalizing the mean field in a harmonic oscillator basis (with $\hbar\omega = 41\ \mathrm{A}^{-1/3}$ MeV), that is, the continuum is discretized. A basis of proton particle-neutron hole plus neutron particle-proton hole configurations is built using all occupied states, as well as the lowest five unoccupied states with increasing values of the radial quantum number n, for each value of (l, j). The RPA matrix equations are solved in this basis, which has been checked to be large enough to ensure that the appropriate sum rules [25] are satisfied. The procedure has already been explained in Ref. [26]. Only the spin-orbit residual two-body force is omitted from the full residual interaction. Because we are mainly interested in the giant resonance region, we neglect the pairing interaction which is expected to have less effect far from the Fermi energy. However, for this reason, our results for the GT strength distribution at low energy should be taken with caution. The nucleus ^{58}Ni is calculated using the filling approximation (that is, four neutrons are in the $p_{3/2}$ subshell with occupation factors 1/2).

Solving the RPA gives the energies E_n of the excited states $|n\rangle$, as well as their wave functions in terms of the $X_{ph}^{(n)}$ and $Y_{ph}^{(n)}$ particle-hole (ph) amplitudes. The corresponding radial transition densities $\delta\varrho$ are given by the following:

$$\delta\varrho_n^{(L)}(r) = \sum_{ph} \left(X_{ph}^{(n)} - Y_{ph}^{(n)}\right) \langle p||A_{JLM}||h\rangle R_p(r) R_h(r), \quad (8)$$

where $R(r)$ is the radial part of the single-particle wave function and A_{JLM} is either Y_{JM} or $[Y_L \otimes \sigma]_{JM}$.

These transition densities are related to the strength of each state S_n associated with the multipole operators (4) and (5) by the following:

$$S_n = |A_n|^2 = \left| \int dr\, r^{L+2} \delta\varrho_n^{(L)}(r) \right|^2. \quad (9)$$

The wave functions of the RPA states $|n\rangle$ are transformed to comply with the DWBA98 code conventions and input into the reaction calculation. In our procedure, we have chosen to average the RPA states lying within a given 1 MeV bin. The averaging is done by using the transition amplitude A_n. This means that the cross section associated with a given energy bin is obtained by using a DWBA calculation that employs a wave function characterized by the amplitudes

$$X_{ph} = \frac{1}{\mathcal{N}} \sum_n A_n X_{ph}^{(n)},$$

where the normalization factor is $\mathcal{N} = \sqrt{\sum_n A_n^2}$, the sum is over the states lying within the bin, and the form of the Y amplitudes is obtained in the same way. The X and Y amplitudes smaller (in absolute value) than 10^{-3} are neglected.

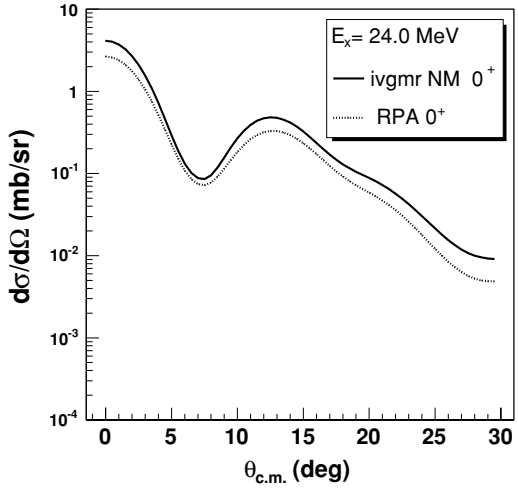

FIG. 4. 0^+ angular distribution in the IVGMR region calculated for the ^{58}Ni(t,^{3}He)^{58}Co reaction. Because of the different normalization of the form factor, the comparison between NM and RPA is made to illustrate their difference in shapes.

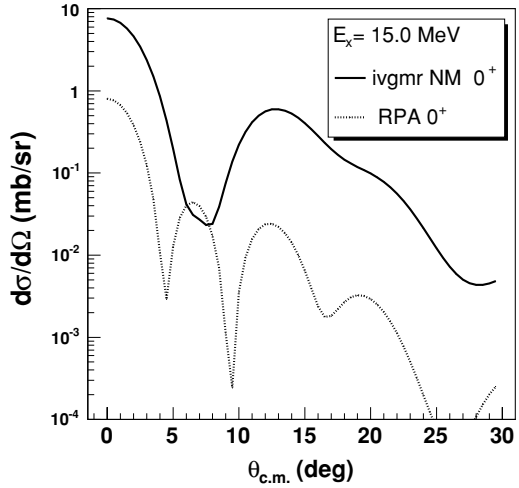

FIG. 5. 0^+ angular distribution for a noncollective excitation calculated for the ^{58}Ni(t,^{3}He)^{58}Co reaction. The comparison between NM and the noncollective RPA excitations is made to illustrate the difference in their angular distributions.

C. Comparison of the angular distributions calculated with the NM and the RPA methods

The strong correlation between the excitation energy and the collectivity of the final states is absent in the NM standard analysis. This correlation affects the form factors and consequently the shape and the amplitude of the calculated cross-section angular distributions. The first very interesting, and indeed expected, feature of RPA angular distributions for collective states is that they have a shape comparable to that of the NM ones, as in the example shown in Fig. 4. This agreement validates the coherence between the phase conventions adopted in NM and RPA in addition to previous tests made on simpler cases with the DWBA98 code.

NM and RPA angular distributions may have different shapes, for example, for the 1^+ states simply because of the mixing in the RPA final state between the $L = 0$ and $L = 2$ transitions. In fact, these two contributions are not separable in the RPA where only J^π is a good quantum number.

The important fact is that for less collective states RPA calculations give a very different shape than the NM form factor even if both L and J are the same. This difference is because of the wave function of the state. The results of the sample calculations are shown in Fig. 5.

By definition, the normal mode form factors overestimate cross sections for noncollective states. These less collective states are observed at a lower excitation energy than the collective ones.

IV. STANDARD NM-MDA AND DWBA+RPA ANALYSIS RESULTS IN THE CASE OF ^{58}NI

A. Standard NM-MDA and indirect comparison with RPA strength calculations

We present first the standard analysis for ^{58}Ni to further compare it with our new analysis including RPA.

After having calculated the angular distributions with the NM wave functions, the NM-MDA analysis requires the minimization of the function

$$\chi^2 = \sum_i \left\{ \left[\sigma_{\rm exp}(\theta_i) - \sum_L \alpha_L \sigma_{\rm th}^L(\theta_i) \right] \Big/ \Delta\sigma_{\rm exp}(\theta_i) \right\}^2 ,$$

where $\sigma_{\rm th}^L$ are the DWBA-calculated differential cross sections with NM wave functions, with the constraint that the α_L coefficients that have to be determined are positive, and taking into account the statistical experimental errors. Here, the index I runs over the scattering angles and the minimization procedure is made separately for the same excitation energy bin at each of these angles. We stress here that the decomposition over L rather than over J is constrained by the limited number of experimental angle measurements and the necessity for the fit to converge. This is usually justified because angular distributions for different J have more or less the same shape for a given L. This is in general rather true with a macroscopic form factor but not always, and it introduces another uncertainty.

We have made such an MDA analysis in the case of the ^{58}Ni target. The spectra were subdivided into 1-MeV-wide bins in the region between 7 and 30 MeV excitation energy and the angular distributions were fitted using combinations of two, three, or four different L. The minimization bin per bin has the advantage over Gaussian or Lorentzian decompositions of not making any *a priori* hypothesis on the final shape of the excitation energy distributions. The $L = 1$ and $L = 2$ contributions were summed over spin-flip and non-spin-flip transitions for all final J^π states, calculated or interpolated at the correct excitation energy, to reduce the number of contributions. In practice, it was impossible to ignore the $L = 2$ contribution in the minimization procedure and the largest uncertainty in the results concerns the non-spin-flip $L = 0$ contribution because of the fact that its integrated

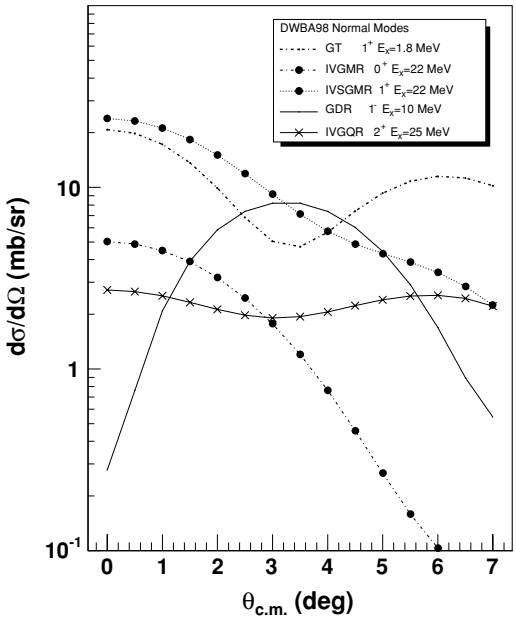

FIG. 6. Typical angular distributions calculated for different L transitions with normal mode wave functions for ^{58}Co excited states.

calculated cross section is very small compared to the spin-flip $L = 0$ one.

We present in Fig. 6 typical angular distributions for different L transitions that illustrate in the case of normal mode wave functions the selectivity of the (t,^{3}He) reaction.

Figure 7 shows the results of the fits at each angle in the case of ^{58}Ni with four combinations where spin-flip and non-spin-flip transitions were distinguished for $L = 0$, but where sums were used for $L = 1$ and $L = 2$. In the 7- to 25-MeV excitation energy region, the cross sections are rather well reproduced. We have obtained large chi-square values at low excitation energy because of a hydrogen impurity and large chi-square values above $E_x = 25$ MeV because of experimental cuts for angles 3 and 4. At other angles the chi-squares of the fits are small. We recall here that up to $E_x = 7$ MeV only the GT levels are essentially expected as previously measured in other experiments and that we have not reanalyzed this region in detail except the 1^+ levels group around $E_x = 1.8$ MeV for making the optical potential choice.

We want to stress here the fact that the globally good convergence of the fit is not a proof that all the deduced α_L are physically meaningful.

In a second step, the resulting α_L distributions are compared with RPA-calculated strength distributions and the sum over all excitation energy bins should provide the fraction of non-energy-weighted sum rule (NEWSR). Therefore, the fraction of NEWSR should have a value of 1 if the strength is totally exhausted in the considered excitation energy range. RPA calculations show that little strength is expected above $E_x = 30$ MeV in ^{58}Co.

Figure 8 shows the resulting ($L = 0$, $S = 1$) and $L = 1$ α_L distributions compared to 1^+ and 1^- RPA strength distributions, respectively. The ($L = 0$, $S = 1$) strength is found fragmented and the detailed comparison between MDA and RPA is not easy. Because of its very small relative contribution

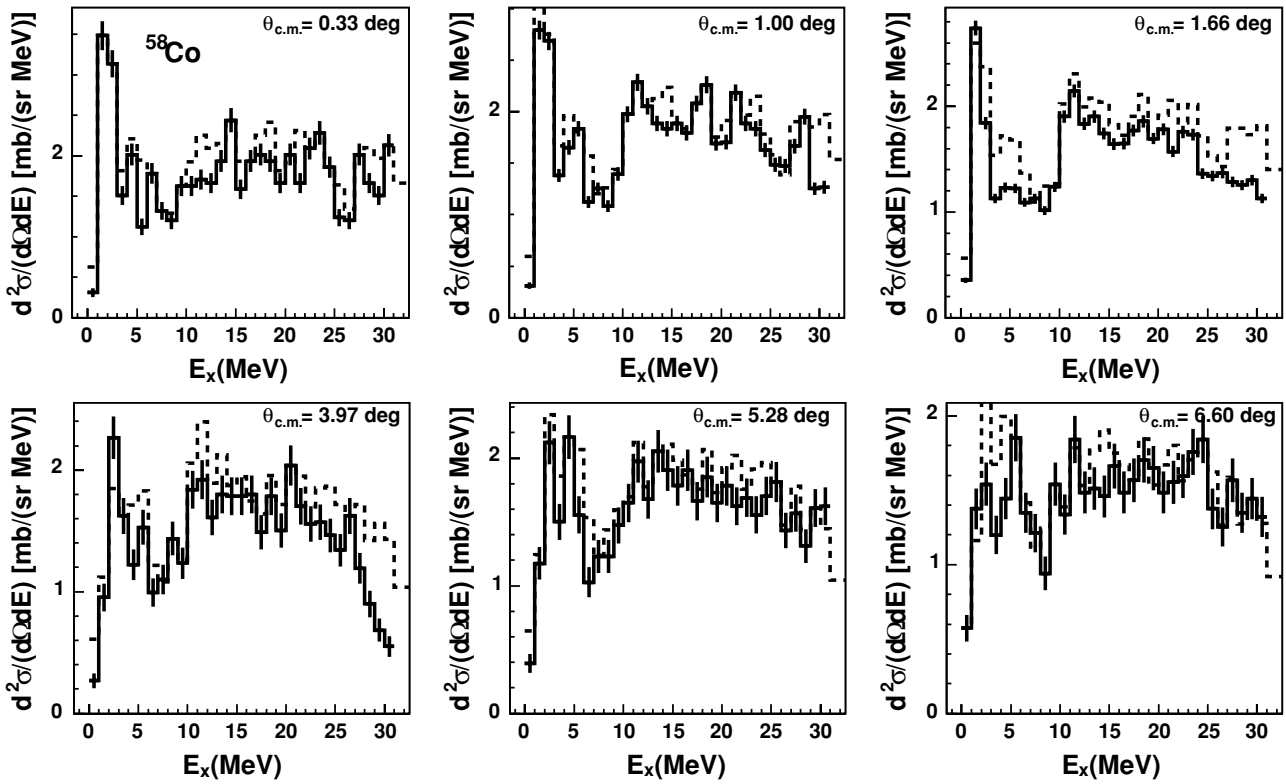

FIG. 7. Results of the fitting procedure at the six measured angles in the case of ^{58}Co. Full lines are binned experimental data and dashed lines are MDA fits obtained with NM wave functions. See text for details.

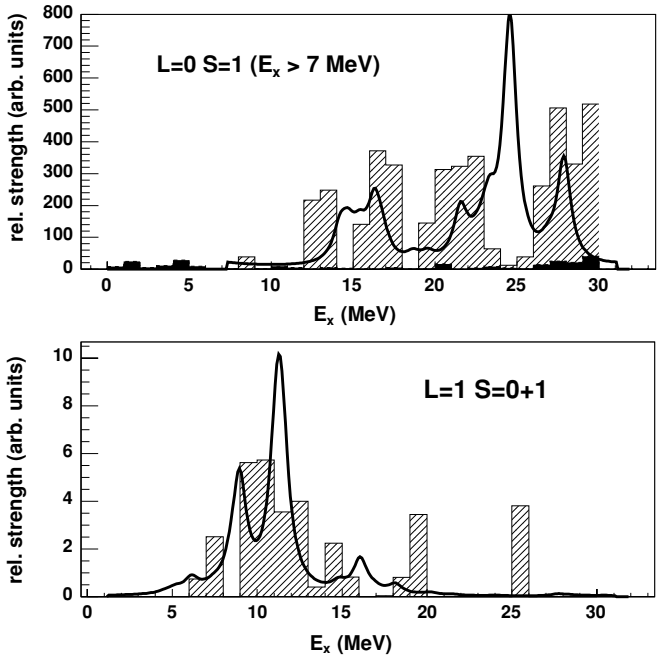

FIG. 8. Comparison between the NM-MDA results (hatched histograms) and the RPA strength calculations (curves) in ^{58}Ni. For $L = 0$ the thick curve represents the ($L = 0$, $S = 1$) transitions above 7 MeV (GT transitions excluded). For $L = 1$, the thick curve represents the 1^-, including both IVGDR+IVSGDR contributions (see text). The small black histogram shows the χ^2 of the MDA fits that are large for excitation energies under 6 MeV and above 25 MeV.

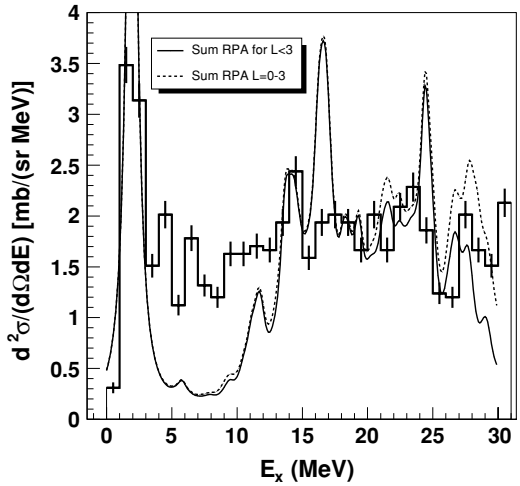

FIG. 9. Comparison between experiment (histogram with statistical error bars) and RPA+DWBA cross-sections (curves) for the ^{58}Ni(t,^{3}He)^{58}Co reaction at 0.5°. The curves correspond to sums of J^π states calculated with set I effective interaction. The dotted curve includes the 2^-, 3^-, and 4^- final states omitted in the full curve.

in particular at larger angles, the ($L = 0$, $S = 0$) deduced strength distribution was the most doubtful because its low contribution in the fit induces an overestimation of its weight in the fit and this has not been presented here. The $L = 1$ strength distribution seems to agree rather well with the 1^- RPA strength. This is all that can be extracted from the present MDA analysis. The microscopic analysis presented in the next section suggests that the MDA deduced peak at $E_x = 19$ MeV in the $L = 1$ spectrum may correspond to a 0^- state. Otherwise, RPA calculations show a 2^- strength maximum around $E_x = 14$ MeV and no L=1 strength above $E_x = 22$ MeV (see Fig. 10).

Table III gives the sum between 7 and 30 MeV for $L = 0$ to $L = 2$ contributions for ^{58}Co with the two effective interaction sets. If all the corresponding strength was found there, this sum should be equal to unity. We note that because the $L = 2$ contribution by default takes into account every higher L, or any possible other mechanism such as quasifree scattering whose angular distribution should be essentially flat in the studied angular range, it is then not surprising that the $L = 2$ sum exceeds unity.

Because of the uncertainty on its extraction linked to the small calculated cross sections, we do not discuss the ($L = 0$, $S = 0$) strength. But the conclusion at this stage of the analysis is that we seem to observe an important quenching of the strength for $L = 1$ ($S = 0 + S = 1$) and also a quenching for ($L = 0$, $S = 1$) compared to the NM strength that is the most collective.

Of course, the relative lower quenching with set II of the effective interaction for ($L = 0$, $S = 1$) is directly linked to the very small value of $V_{\sigma\tau}$, which is somewhat in contradiction with the fact that in the *NN* interaction we know that at this energy per nucleon V_τ and $V_{\sigma\tau}$ should have comparable values. There is missing strength in both cases. This preliminary conclusion is in accordance with our previous remark that NM wave functions overestimate the collectivity of certain states.

B. Global direct comparisons of DWBA+RPA and experimental differential cross sections

A smoothing was made over all the states of equal J^π, individually calculated with the DWBA98 code, by a convolution with a Lorentzian of 1 MeV width to construct a theoretical spectrum that could be more easily compared at each angle with the experimental one.

The experimental and calculated spectra are compared for the ^{58}Co nucleus at 0.5° in Fig. 9.

TABLE III. Deduced sums for $L = 0$ to $L = 2$ strengths for the ^{58}Co nucleus.

Effective	V_τ	$V_{\sigma\tau}$	$V_{T\tau}$	Sum over [7–30 MeV]		
interaction set	(MeV)	(MeV)	(MeV)	($L = 0$, $S = 1$)	$L = 1$	$L = 2$
I	5.00	−4.10	−6.00	0.362	0.209	1.202
II	5.00	−3.00	−6.50	0.565	0.240	1.170

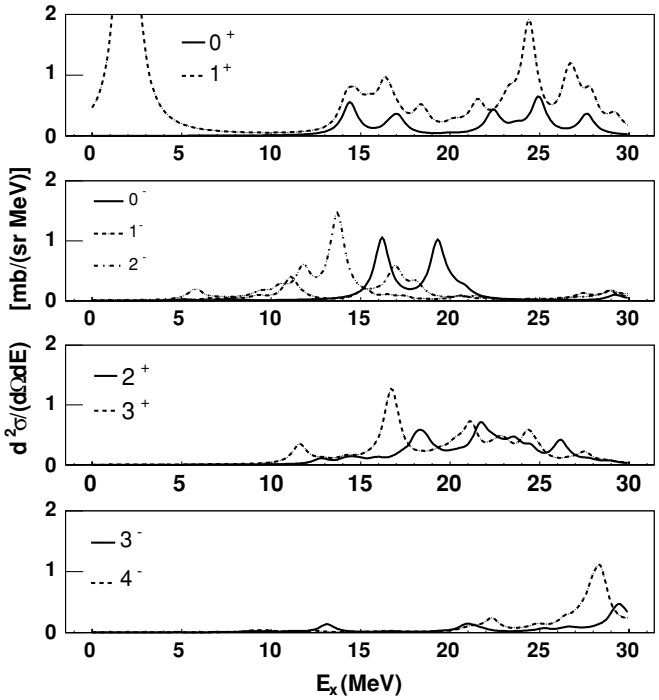

FIG. 10. Different RPA J^π contributions to the cross section at 0.5° with set I effective interaction for the ^{58}Ni(t,^{3}He)^{58}Co reaction.

We stress that the spectra are compared on an absolute differential cross-section scale without any renormalization factor. Of course, as we expect, we can see that the present RPA calculations predict less spreading than is experimentally observed and this is because of the neglect of escape and spreading (coupling with $2p-2h$) widths. At low excitation energy, the discrepancy between the experimental and calculated spectra is because of the neglect of pairing in RPA calculations. Previous experiments have already revealed GT strength over 4 MeV excitation energy. At higher excitation energy this comparison shows that we do not need to invoke extra sequential mechanisms or quasifree scattering to reproduce the globally observed cross sections, but that we have to add higher-order multipolarities in the framework of the direct charge-exchange mechanism.

The spectra calculated for different J^π are presented in Fig. 10, grouped as a function of their alternating parities and of their J values that mainly reflect the dominant L transitions ($L = 0$, 1, 2, or 3). We can further stress from examining Fig. 9 that it is necessary to add $L = 3$ contributions (2^-, 3^-, 4^- states) to reproduce the experimental spectra better, but only above $E_x = 25$ MeV.

C. Comparison of energy-integrated cross sections

Although standard NM-MDA results in an apparent strong quenching of the strength, because NM calculations overestimate the collectivity of the form factor with both phenomenological effective interactions presently used, the global comparison with the DWBA+RPA calculated spectra indicates that the experimental energy-integrated cross section seems to agree with the calculated one, as shown in Table IV. In this table, we have directly compared for each angle the integrated (summed over 1 MeV bins) experimental and calculated DWBA+RPA cross sections over 7–30 MeV (thus excluding the GT resonance region) for ^{58}Co. The calculated DWBA+RPA cross sections include all J^π states corresponding to spin-flip and non-spin-flip transitions for $L =$ 0, 1, 2, and 3. This table also provides the ratio between the experimental and calculated value. It shows that within ±20% the integrated cross section is reproduced for ^{58}Co without invoking any mechanism other than direct charge-exchange.

D. Evidence for the monopole resonance

Because $L = 0$ angular distributions are peaked at very forward angles, in contrast to $L = 1$ that have a minimum there, and because any higher multipolarity or more complex mechanism than direct charge-exchange should have flatter angular distributions in the measured angular range, it is interesting to compare the difference between spectra at angle 1 and angle 4 (see Fig. 6). This difference spectrum should enhance $L = 0$ structures. Figure 11 shows the experimental and calculated difference spectra, where in the calculated spectra the two curves concern 0^+ (full curve) and 1^+ (dotted curve) states only. We stress that they are expressed in absolute values in mb/(sr MeV). We can conclude that the global agreement for $L = 0$ is striking. Unfortunately, experimental difference spectra cannot be extracted from excitation energies above 25 MeV because of an experimental cut for the angle 4 spectrum.

The same subtraction can be done to try to locate the $L = 1$ concentrations. In this case, the better choice is to subtract the angle 1 spectrum from that of angle 3 (see Fig. 6) and to look at the positive part of this difference. This is shown in Fig. 12, where the comparison is made with 1^- calculation in the case of the set I effective interaction. The agreement in position, around 11.5 MeV, is rather good despite the fact that we are at

TABLE IV. Ratios of integrated cross sections at every measured angle for ^{58}Ni target nucleus.

Integrated cross section	Angle 1	Angle 2	Angle 3	Angle 4	Angle 5	Angle 6
Experimental (mb/sr)	53. ± 1.4	52. ± 0.8	45. ± 0.6	44. ± 1.4	48. ± 1.4	43. ± 1.4
RPA set I (mb/sr)	43.	45.	47.	52.	49.	45.
Ratio	1.23	1.15	0.96	0.85	0.98	0.96
RPA set II (mb/sr)	51.	53.	55.	56.	52.	45.
Ratio	1.04	0.98	0.82	0.79	0.92	0.96

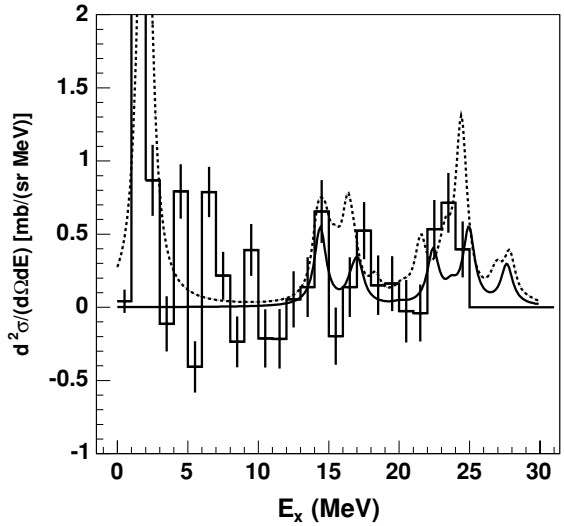

FIG. 11. Comparison between the difference experimental spectra (histograms with error bars) and difference RPA calculated differential cross sections for 0^+ (full curve) and 1^+ (dotted curve) final states both obtained by subtracting the angle 4 spectrum from that of angle 1 in the case of the ^{58}Co nucleus.

a low incident energy, which is not the best suited for exciting these states dominated by $L = 1$ transitions. The agreement obtained with the set II effective interaction is comparable.

V. RESULTS OF THE DWBA+RPA ANALYSIS IN THE CASE OF ^{48}K NUCLEUS

For this nucleus, we present only the results from the new DWBA+RPA analysis. Experimental and calculated spectra are compared in Fig. 13. The filling of the $1f_{7/2}$ shell in the

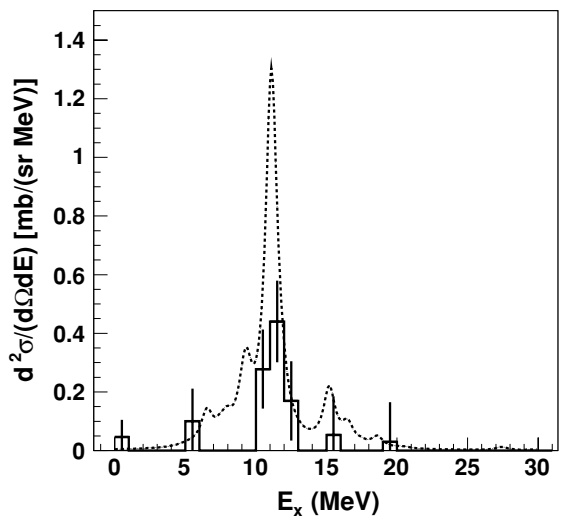

FIG. 12. Comparison between the positive difference experimental spectra (histograms with error bars) and difference RPA calculated differential cross sections for 1^- (dotted curve) final states both obtained by subtracting angle 1 spectrum from that of angle 3 in the case of the ^{58}Co nucleus.

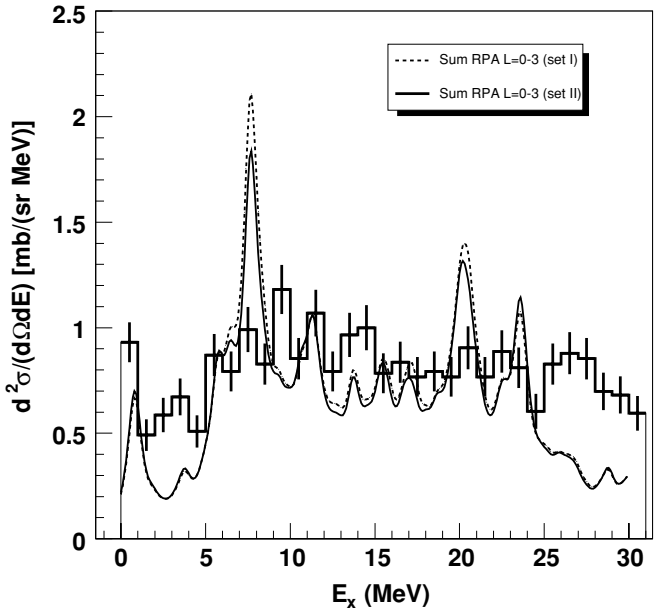

FIG. 13. Comparison between experiment (histogram with statistical error bars) and RPA (curves) for the ^{48}Ca(t,^{3}He)^{48}K reaction at 0.5°. The curves correspond to sums of J^π states calculated with the set I (dashed curve) and the set II (dotted curve) effective interactions, respectively.

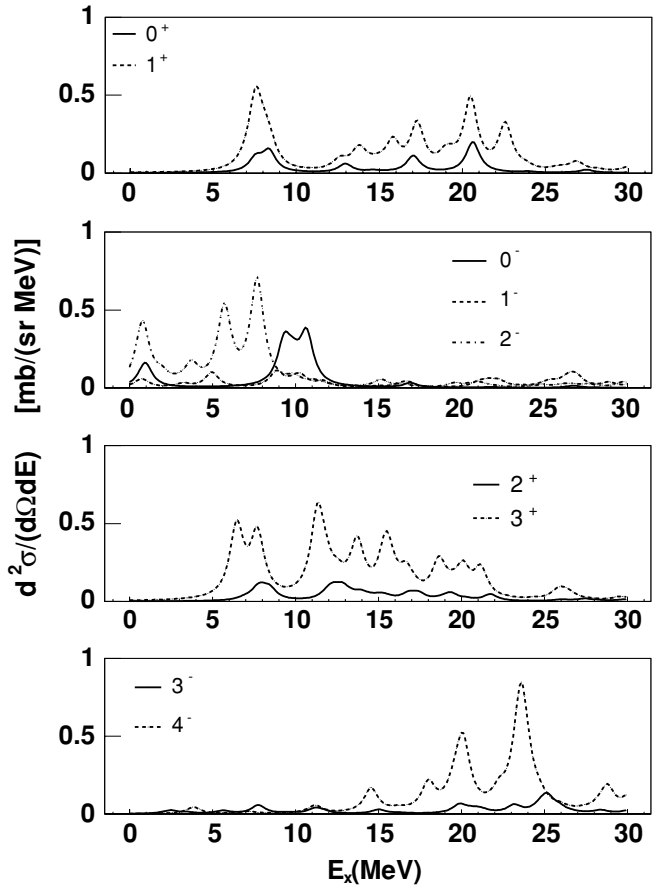

FIG. 14. Different RPA J^π contributions to the cross section at 0.5° in mb/(sr MeV) with set I effective interaction for the ^{48}Ca(t,^{3}He)^{48}K reaction.

TABLE V. Ratios of integrated cross sections at every measured angle for the ^{48}Ca target nucleus.

Integrated cross section	Angle 1	Angle 2	Angle 3	Angle 4	Angle 5	Angle 6
Experimental (mb/sr)	20. ± 0.4	19. ± 0.3	18. ± 0.2	18. ± 0.3	18. ± 0.3	15. ± 0.3
RPA set I (mb/sr)	18.	19.	20.	19.	17.	15.
Ratio	1.11	1.00	0.9	0.95	1.06	1.00
RPA set II (mb/sr)	18.	18.	19.	19.	17.	16.
Ratio	1.11	1.06	0.95	0.95	1.06	0.94

^{48}Ca target prevents the excitation of GT strength and higher multipole excitations are at a lower excitation energy compared to the case of ^{58}Ni. Adding $L = 4$ strength would probably fill the calculated spectra above 25 MeV. The different calculated multipolarities are presented in Fig. 14 and we can observe that $L = 0$ and $L = 2$ energy distributions are again largely spread out over the excitation energy range.

Table V also shows that here again, within ±10%, the integrated cross section between excitation energies between 0 and 25 MeV is reproduced for ^{48}K without any mechanism other than direct charge exchange.

The difference spectra shown in Fig. 15 compare less favorably than in the ^{58}Co case (see Fig. 11) in the low-excitation region (some shift appears between 7 and 9 MeV for the main structure) but experimental and calculated spectra agree in the region around 20 MeV, where we would expect the monopole resonance. We stress that in this excitation energy region angular distributions calculated with NM or RPA form factors are again very similar, pointing to the collective nature of these structures.

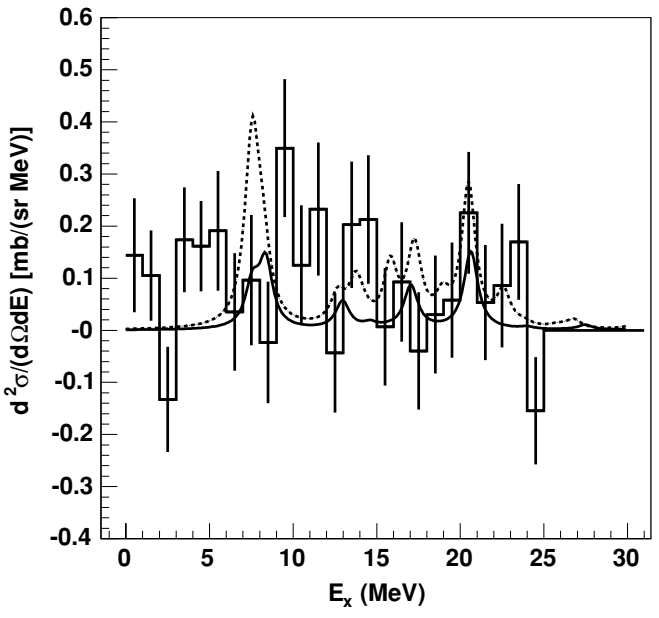

FIG. 15. Comparison between the difference experimental spectra (histograms with error bars) and difference RPA calculated differential cross sections for 0^+ (full curve) and 1^+ (dotted curve) final states both obtained by subtracting angle 4 spectrum from that of angle 1 in the case of ^{48}K nucleus.

VI. CONCLUSIONS

We have presented a microscopic analysis of the (t,^{3}He) reaction measured on ^{48}Ca and ^{58}Ni targets. The calculated spectra, including all final J^π RPA states, reproduce the measured cross sections globally very well at every angle. The integrated cross sections between 0 and 30 MeV are in very good agreement. In the case of $L = 0$ transitions on a ^{58}Ni target the main structures are comparable. If we characterize a collective state by the fact that NM and RPA give the same angular distribution shape, we can even deduce from the present new analysis where the main collective and noncollective structures are. In the case of the presently studied medium-weight nuclei there is certainly not a single collective state, but a pronounced fragmentation of all multipole strengths. The subtraction of spectra for appropriate angle pairs helps in locating the energy distributions in the cases of $L = 0$ and $L = 1$ transitions and the agreement between theory and experiment is good. This method is, of course, not adapted for higher L because their angular distributions are flat in the region investigated in the present experiment. These higher L contributions, particularly $L = 3$, are necessary to reproduce the cross sections at a high excitation energy.

These conclusions should be confirmed on heavier nuclei such as ^{90}Zr and ^{208}Pb, because RPA calculations are even better suited to describing the nuclear structure of such nuclei. An improvement of the mechanism description could come from the use of a more realistic effective projectile-N interaction, taking into account LS and eventually higher-order terms, but also the convolution in the projectile of the exchanged nucleon with the spectator nucleons. Such an improvement would in particular need a detailed study of the free p(t,^{3}He)n reaction at our incident energy. In other words, a double folding of the transition densities in the target and in the projectile with the NN interaction has to be implemented.

Coming back to the long-standing question concerning the monopole strength distribution, we can draw two conclusions from the present analysis. First, in these two nuclei, the strengths of different multipolarities are strongly overlapping. Second, the $L = 0$ strength is fragmented into two main regions. The most collective one, located in excitation energies around 24 to 27 MeV, can be identified as the monopole resonance and a less collective contribution located around 15 MeV in ^{58}Co. The collective resonance is around 20 MeV in ^{48}K, whereas lower excitation energy contributions are less distinguishable. In conclusion of this analysis, we can understand the reason why it was so difficult to identify the monopole strength in this mass region in previous experiments

because it does not dominate the spectra except at 0°. This is true even in the case of the present $(t,{}^3\mathrm{He})$ at rather low incident energy that nevertheless seemed to be better suited than others for this purpose. The method that we have employed here, using DWBA+RPA calculations and a direct comparison between calculated and measured spectra, is much more relevant for disentangling the different multipolarities in such nuclei than previous fitting procedures.

ACKNOWLEDGMENTS

Part of this work was supported by the Large-Scale Facility LIFE (E.U.) contract HPRI-CT-1999-00109 and it has been performed in the framework of a CNRS/IN2P3-FSR/FOM collaboration. We acknowledge particularly the AGOR staff members and the KVI collaborators for the excellent operation of AGOR during the experiment.

[1] M. N. Harakeh and A. van der Woude, *Giant Resonances: Fundamental High-Frequency Modes of Nuclear Excitation* (Oxford University Press, Oxford, 2001), and references therein.
[2] T. Ichihara, M. Ishihara, H. Ohnuma, T. Niizeki, Y. Satou, H. Okamura, S. Kubono, M. H. Tanaka, and Y. Fuchi, Phys. Rev. Lett. **89**, 142501 (2002) and references therein.
[3] R. G. T. Zegers *et al.*, Phys. Rev. Lett. **90**, 202501 (2003).
[4] H. Sakai *et al.*, Nucl. Phys. **A654**, 731 (2003).
[5] W. G. Love and M. A. Franey, Phys. Rev. C **24**, 1073 (1981).
[6] S. Brandenburg *et al.*, AIP Conf. Proc. **600**, 463 (2001).
[7] A. M. van den Berg, Nucl. Instrum. Methods B **99**, 637 (1995).
[8] M. de Huu, Ph.D. thesis, University of Groningen, 2004.
[9] J. Raynal, DWBA98 Computer Program, NEA-1209/05, IAEA.
[10] S. Y. van der Werf *et al.*, Nucl. Phys. **A496**, 305 (1989).
[11] A. Djaloeis and S. Gopal, Nucl. Phys. **A356**, 97 (1981).
[12] M. Hyakutake *et al.*, Nucl. Phys. **A333**, 1 (1980).
[13] S. L. Tabor, C. C. Chang, M. T. Collins, G. J. Wagner, J. R. Wu, D. W. Halderson, F. Petrovich, Phys. Rev. C **25**, 1253 (1982).
[14] T. Nakamura *et al.*, Phys. Lett. **B493**, 209 (2000).
[15] R. Schaeffer, Nucl. Phys. **A164**, 145 (1971).
[16] R. Zegers, Ph.D. thesis, University of Groningen, 1999.
[17] S. Cohen and D. Kurath, Nucl. Phys. **73**, 1 (1965).
[18] S. Y. van der Werf, Phys. Scr. T **32**, 43 (1990).
[19] T. Kawabata (private communication).
[20] S. Y. van der Werf, computer code NORMOD, unpublished.
[21] M. Hofstee *et al.*, Nucl. Phys. **A588**, 729 (1995).
[22] A. Kolomiets, O. Pochivalov, and S. Shlomo, Phys. Rev. C **61**, 034312 (2000).
[23] G. Colò and N. Van Giai, Nucl. Phys. **A731**, 15 (2004).
[24] G. Colò, S. M. Lenzi, E. E. Maqueda, and A. Vitturi, Phys. Rev. C **67**, 044306 (2003).
[25] N. Auerbach and A. Klein, Nucl. Phys. **A395**, 77 (1983).
[26] G. Colò, N. Van Giai, P. F. Bortignon, and R. A. Broglia, Phys. Rev. C **50**, 1496 (1994).
[27] N. Van Giai and H. Sagawa, Phys. Lett. **B106**, 379 (1981).